ADVANCED MATERIALS
www.advmat.de

Enhanced CO_2 Electrolysis Through Mn Substitution Coupled with Ni Exsolution in Lanthanum Calcium Titanate Electrodes

*Nuoxi Zhang, Aaron Naden, Lihong Zhang, Xiaoxia Yang, Paul Connor, and John Irvine**

In this study, perovskite oxides $La_{0.3}Ca_{0.6}Ni_{0.05}Mn_xTi_{0.95-x}O_{3-\gamma}$ ($x = 0$, 0.05, 0.10) are investigated as potential solid oxide electrolysis cell cathode materials. The catalytic activity of these cathodes toward CO_2 reduction reaction is significantly enhanced through the exsolution of highly active Ni nanoparticles, driven by applying a current of 1.2 A in 97% CO_2 – 3% H_2O. The performance of $La_{0.3}Ca_{0.6}Ni_{0.05}Ti_{0.95}O_{3-\gamma}$ is notably improved by co-doping with Mn. Mn dopants enhance the reducibility of Ni, a crucial factor in promoting the in situ exsolution of metallic nanocatalysts in perovskite (ABO_3) structures. This improvement is attributed to Mn dopants enabling more flexible coordination, resulting in higher oxygen vacancy concentration, and facilitating oxygen ion migration. Consequently, a higher density of Ni nanoparticles is formed. These oxygen vacancies also improve the adsorption, desorption, and dissociation of CO_2 molecules. The dual doping strategy provides enhanced performance without degradation observed after 133 h of high-temperature operation, suggesting a reliable cathode material for CO_2 electrolysis.

1. Introduction

The rapid growth of energy consumption from fossil fuel sources has led to the energy crisis and environmental deterioration. These issues emerge due to the rising global energy demand, over-reliance on fossil fuels and significant emission of greenhouse gas CO_2.[1]

Within this context, solid oxide electrolysis cells (SOECs) operating at high temperature (600–1000 °C) have emerged as a potential solution for CO_2 utilization. Their ability to efficiently convert renewable electrical energy into low-carbon fuels, coupled with high Faraday efficiency and fast kinetics of CO_2 reduction reaction, place them at the forefront of promising technologies.[2–4] In this process, CO_2 undergoes direct electrolysis via SOECs producing CO that can be further converted into high-value products, such as liquid fuels via the Fischer–Tropsch synthesis.[5,6] This approach not only provides an effective solution for energy storage but also significantly mitigates the environmental impact of CO_2.

Ni-based cermets, such as Ni-YSZ (yttria-stabilized zirconia) are state-of-the-art cathode materials in SOECs for CO_2 electrolysis, owing to their remarkable electro-catalytic activity, excellent electrical conductivity, relatively high mechanical strength, and low cost. However, Ni-based cermets suffer from several disadvantages that hinder their further application, for example, volume instability on redox cycling, agglomeration of metal phase during prolonged usage, and deactivation of Ni by carbon deposition.[7,8]

Perovskite oxides (ABO_3) have been proposed as alternative fuel electrodes to the Ni-based cermets due to their high electrical conductivity and good chemical stability upon redox cycling.[9,10] Nonetheless, the intrinsic catalytic activity of perovskite oxides is significantly inferior to that of traditional Ni-based cermets. In recent years, enhancing the catalytic activity of perovskite oxides has been achieved through surface modification, employing metal or alloy nanoparticles as synergistic catalysts.[11] Impregnation and in situ exsolution are two approaches typically used for this purpose. The conventional impregnation method involves introducing a precursor solution into a porous perovskite scaffold, followed by thermal treatment to form catalytic nanoparticles. However, this method is time-consuming due to the necessity for multiple complex deposition steps. In addition, this technique offers limited control over the size and distribution of the deposited nanoparticles. The nanoparticles deposited through this process also tend to agglomerate and coarsen during long-term operations at high temperatures.[12,13]

A more promising and efficient alternative, in situ exsolution, has been developed. This approach involves incorporating active metal elements as B-site dopants into the lattice of the perovskite

N. Zhang, A. Naden, L. Zhang, X. Yang, P. Connor, J. Irvine
School of Chemistry
University of St Andrews
St Andrews KY16 9ST, UK
E-mail: jtsi@st-and.ac.uk
L. Zhang, X. Yang
Beijing Key Laboratory for Chemical Power Source and Green Catalysis
Beijing Institute of Technology
Beijing 100081, P. R. China

The ORCID identification number(s) for the author(s) of this article can be found under https://doi.org/10.1002/adma.202308481

DOI: 10.1002/adma.202308481

oxides during the sample preparation stage in the air. These elements are then exsolved from the perovskite-based oxide matrix to form metal nanoparticles on the surface, either by exposure to a reducing atmosphere or by applying a large cathodic overpotential. Compared with conventional impregnation, the exsolved nanoparticles are uniformly distributed and anchored to the parent perovskite. These exsolved nanoparticles demonstrate outstanding resistance to agglomeration and coking, benefiting from the strong interfacial interaction between the oxide matrix and the nanoparticles. The interface between exsolved metal nanoparticles and the perovskite oxides exhibits catalytic activity.[3,14,15] Irvine et al. reported that A-site deficiency could serve as a general driving force to initiate B-site exsolution.[16] The oxygen vacancies created due to A-site deficiency could partially destabilize the perovskite lattice. This destabilization could then locally trigger the spontaneous exsolution of B-site elements as an attempt to maintain the charge balance of the perovskite lattice, and thus facilitating the in situ exsolution process. Numerous researchers have demonstrated that an A-site deficiency can significantly enhance the performance of solid oxide cells.[17–19] Furthermore, Irvine et al. demonstrated that the voltage-driven reduction method could produce notably richer metal nanoparticles compared to the chemical reduction method. The cell treated using the voltage-driven reduction method under conditions of 2 V for 150 s in 50% H_2O/N_2 exhibits outstanding electrochemical performance relative to those treated with chemical reduction methods, which involve reducing in 5% H_2/N_2 for over 17 h.[20]

CO_2 electrolysis through solid oxide cells suffers from the insufficient adsorption and activation of CO_2 molecules, which can be attributed to the intrinsic properties of the stable and linear C═O bond.[21,22] Introducing oxygen vacancies, which could act as host sites to accommodate the linear CO_2 molecules, has been considered as an effective method to enhance the surface adsorption and activation of these molecules. Additionally, these oxygen vacancies could function as charge carriers for O^{2-} transfer, leading to an increase in both the oxygen ionic conductivity and the oxygen ion diffusion through the electrode.[2] To date, numerous studies have demonstrated the beneficial role of Mn in enhancing the catalytic activity of the perovskite fuel electrodes. Irvine et al. demonstrated that introducing redox activity by partially substituting Ti with Ga and Mn allows more flexible coordination, breaks down the extended defect intergrowth regions, and creates phases with considerable disordered oxygen defects.[23] The modified fuel electrode material ($La_4Sr_8Ti_{11}Mn_{0.5}Ga_{0.5}O_{37.5}$) exhibited outstanding fuel cell performance in wet hydrogen at 950 °C, a performance comparable to that of traditional nickel/zirconia cermets. Wu et al. demonstrated that Mn-doped titanate ($La_{0.2}Sr_{0.8}Ti_{0.9}Mn_{0.1}O_{3+\delta}$) not only enhances the ionic conductivity but also notably improves the chemical adsorption of CO_2 molecules. Additionally, it significantly extends the chemical desorption of CO_2 molecules to the high temperature region.[24] Further research by Xie et al. highlighted that cell performance could be improved by co-doping Ni and Mn into the B-site perovskite lattice.[25] They found that $(La_{0.2}Sr_{0.8})_{0.95}Ti_{0.85}Mn_{0.1}Ni_{0.05}O_{3+\delta}$ reached a maximum current density of 0.87A cm^{-2} at 2.0 V at 800 °C in CO_2. This performance surpassed that of $(La_{0.2}Sr_{0.8})_{0.95}Ti_{0.9}Mn_{0.1}O_{3+\delta}$, which achieved a maximum current density of 0.66A cm^{-2} under the same testing conditions. Yet, to the best of our knowledge, the influence of Mn on the exsolution process of perovskite materials remains unexplored.

Herein, we focus on the exploration of the A-site deficient titanate $La_{0.3}Ca_{0.6}Ni_{0.05}Mn_xTi_{0.95-x}O_{3-\gamma}$ (x = 0, 0.05, 0.10) fuel electrodes with various Mn doping levels. Its impact on the structure, morphology, oxygen content, and electrical conductivity was systematically examined. Mn doping results in the creation of more oxygen vacancies and significantly facilitates the Ni exsolution process. In this study, the cells are activated using the electrochemical reduction method, with a current load of 1.2 A. To optimize the cell performance, the role of cathode microstructure and electrochemical reduction in the performance of $La_{0.3}Ca_{0.6}Ni_{0.05}Mn_xTi_{0.95-x}O_{3-\gamma}$ cells is explored. Two key factors are discussed: the direct impact of the cathode microstructure on the cell performance and the influence of the electrochemical reduction process, which is itself affected by the cathode microstructure, on the overall performance of the cells. Finally, cells with similar microstructures are assessed and compared to investigate the impact of Mn doping levels on electrochemical performance. Mn-doped cathode exhibits superior cell performance due to the surface modification with a higher density of exsolved nanoparticles and higher oxygen vacancy concentrations in the oxide matrix. $La_{0.3}Ca_{0.6}Ni_{0.05}Mn_{0.05}Ti_{0.90}O_{3-\gamma}$ achieves a maximum current density of −2.89 A cm^{-2} in a gas mixture of 77.6% CO_2 – 19.4% H_2 – 3% H_2O at 1.8 V and 900 °C. The stability test of the $La_{0.3}Ca_{0.6}Ni_{0.05}Mn_{0.05}Ti_{0.90}O_{3-\gamma}$ electrolysis cell demonstrated good durability during the 133 h operation at 900 °C under an applied voltage of 1.2 V, indicating a promising cathode material for high temperature CO_2 electrolysis.

2. Results and Discussions

2.1. Materials Characterization

Figure 1 shows the XRD patterns of the oxidized and reduced $La_{0.3}Ca_{0.6}Ni_{0.05}Mn_xTi_{0.95-x}O_{3-\gamma}$ (x = 0, 0.05, 0.10) samples. The corresponding Rietveld refinement profiles are also shown in Figure S1 (Supporting Information). The obtained χ^2 values close to 1 suggest an excellent fit, implying that the model accurately represents the experimental XRD data. All oxidized samples exhibit a single perovskite phase with an orthorhombic (*Pnma*) space group. The lattice parameter of the materials increases with the increasing doping level of Mn, which is mainly due to the partial replacement of the Ti^{4+} (0.605 Å) ion by the Mn^{3+} ion (0.645 Å) with a larger radius.[26] After the reduction in the 5% H_2/N_2 at 900 °C for 10 h, the perovskite phase remains as the main phase for all the reduced samples, indicating the synthesized perovskites exhibit good structural stability under the reducing environment. An extra peak located at ≈44.4° is detected for all the reduced samples (see Figure 1c), corresponding to the metallic Ni (*Fm-3m*). The presence of these metallic peaks confirms the successful exsolution process. To further determine the degree of nickel exsolution for each reduced sample, Rietveld refinement of XRD data was performed. The relative amount of Ni is determined to be 0.271 wt%, 0.498 wt%, and 0.789 wt% for $La_{0.3}Ca_{0.6}Ni_{0.05}Ti_{0.95}O_{3-\gamma}$ (LCNT), $La_{0.3}Ca_{0.6}Ni_{0.05}Mn_{0.05}Ti_{0.90}O_{3-\gamma}$ (LCNMT5), and $La_{0.3}Ca_{0.6}Ni_{0.05}Mn_{0.10}Ti_{0.85}O_{3-\gamma}$ (LCNMT10), respectively. This strongly demonstrates that the Mn dopants can promote the exsolution of Ni cation from the perovskite lattice.

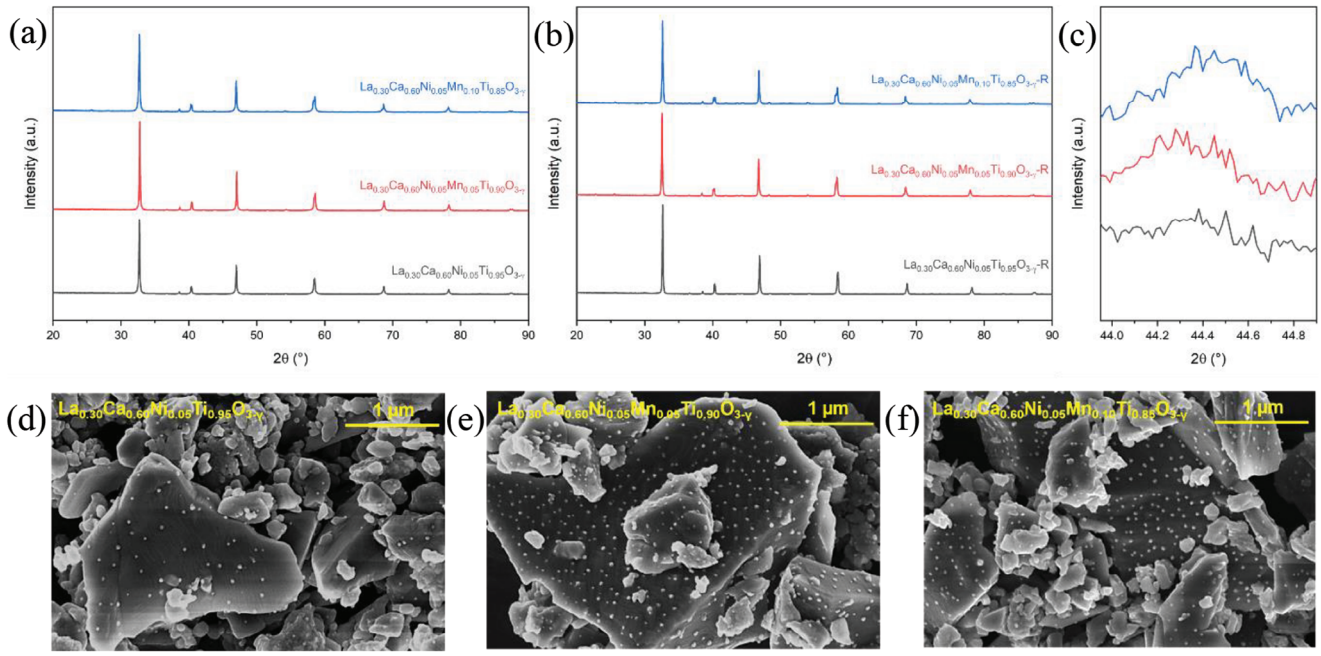

Figure 1. XRD patterns of the $La_{0.30}Ca_{0.60}Ni_{0.05}Mn_xTi_{0.95-x}O_{3-\gamma}$ ($x = 0$, 0.05, 0.10) powders a) as-synthesized, b) reduced in 5% H_2/N_2 at 900 °C for 10 h, and c) with the enlarged 43.95–44.90 2θ range from b). SEM images of reduced d) LCNT, e) LCNMT5, and f) LCNMT10 powders.

This result is consistent with the increased amount of exsolved nanoparticles on the powder surface, as observed in SEM measurement (Figure 1d–f). The observed phenomenon could be attributed to the propensity of Mn to adopt lower coordination numbers within the perovskite lattice.[27] Consequently, this may promote oxide-ion migration,[23] thereby facilitating the exsolution process in the material. The exsolved Ni metal nanoparticles across all samples exhibit a similar size distribution, with an average particle diameter of ≈28 nm. The morphology of the powders before the reduction process is shown in Figure S2 (Supporting Information). In the as-prepared samples, the powder surfaces exhibit a smooth and clear morphology. The presence of small sized particles can be attributed to the ball milling process. These particles possess an irregular shape, contrasting with the rounded shape of the exsolved nanoparticles observed postreduction. Additionally, the lattice volume of the samples exhibit expansion in comparison to the as-prepared materials, as illustrated in Figure S3 (Supporting Information). This phenomenon can be primarily ascribed to the reduction of Ti^{4+} (0.605 Å) to Ti^{3+} (0.670 Å) and Mn^{3+} (0.645 Å) to Mn^{2+} (0.830 Å) within the crystal structure.[26] A more pronounced expansion of the lattice volume is observed for Mn-doped samples. The substantial difference in ionic radii between Mn^{3+} and Mn^{2+} ions contribute to a more significant lattice volume expansion in the Mn-doped samples.

To gain further insight into the crystal structure of both the exsolved nanoparticles and the oxide matrix, a combination of scanning transmission electron microscopy (STEM) and energy-dispersive X-ray spectroscopy (EDX) analysis was carried out. **Figure 2**a presents the dark-field STEM image of the reduced LCNMT5 perovskite powders, revealing numerous exsolved metallic nanoparticles emerging on the surface of the parent particles. Figure 2b illustrates a high-angle annular dark field scanning transmission electron microscopy (HAADF-STEM) image. The exsolved nanoparticles exhibit an interplanar spacing of 1.76 Å, which corresponds to the {020} crystal planes of Ni metal (space group *Fm-3m*). The lattice spacings between the planes of the perovskite substrate are 2.72 and 3.88 Å, aligning with the lattice constants of the {002} and {020} planes in the orthorhombic crystal structure (space group *Pnma*), respectively. In Figure 2c–h, the HAADF-STEM image is presented along with its associated elemental mapping images. The elements of La, Ca, Ti, and Mn are uniformly distributed on the perovskite support, while the Ni nanoparticles are exsolved from the perovskite matrix. These findings are consistent with the above-mentioned XRD analysis. It is essential to highlight that parts of the exsolved nanoparticles are embedded into the parent perovskite, indicating a strong interaction between the titanate backbone and the exsolved nanoparticles. This anchoring effect is expected to improve the thermal stability of the catalyst, effectively preventing the agglomeration of the metal nanoparticles under the operating conditions of SOECs.[13,28–30] Complementary STEM and EDX results for LCNT and LCNMT10 are provided in Figures S4 and S5 (Supporting Information), respectively. It is worth noting that based on the EDX mapping, a weak Mn signal is detected around the Ni nanoparticles for both LCNMT5 and LCNMT10 samples, suggesting a possibility of Mn exsolution. However, further examination using an EDX line scan demonstrates that the intensity of the Mn signal remains nearly uniform across the exsolved nanoparticles and the perovskite substrates (Figure 2i; and Figure S5i, Supporting Information). Given the uniformity in Mn signal intensity, it becomes challenging to ascertain this. While there is a possibility of Mn exsolution around the Ni nanoparticles, its presence seems minimal. Supporting this observation, no Mn metal or MnO_x peaks are detected in the XRD results, indicating that any exsolved Mn metal or MnO_x, if present, likely has a minimal impact on the cell performance.

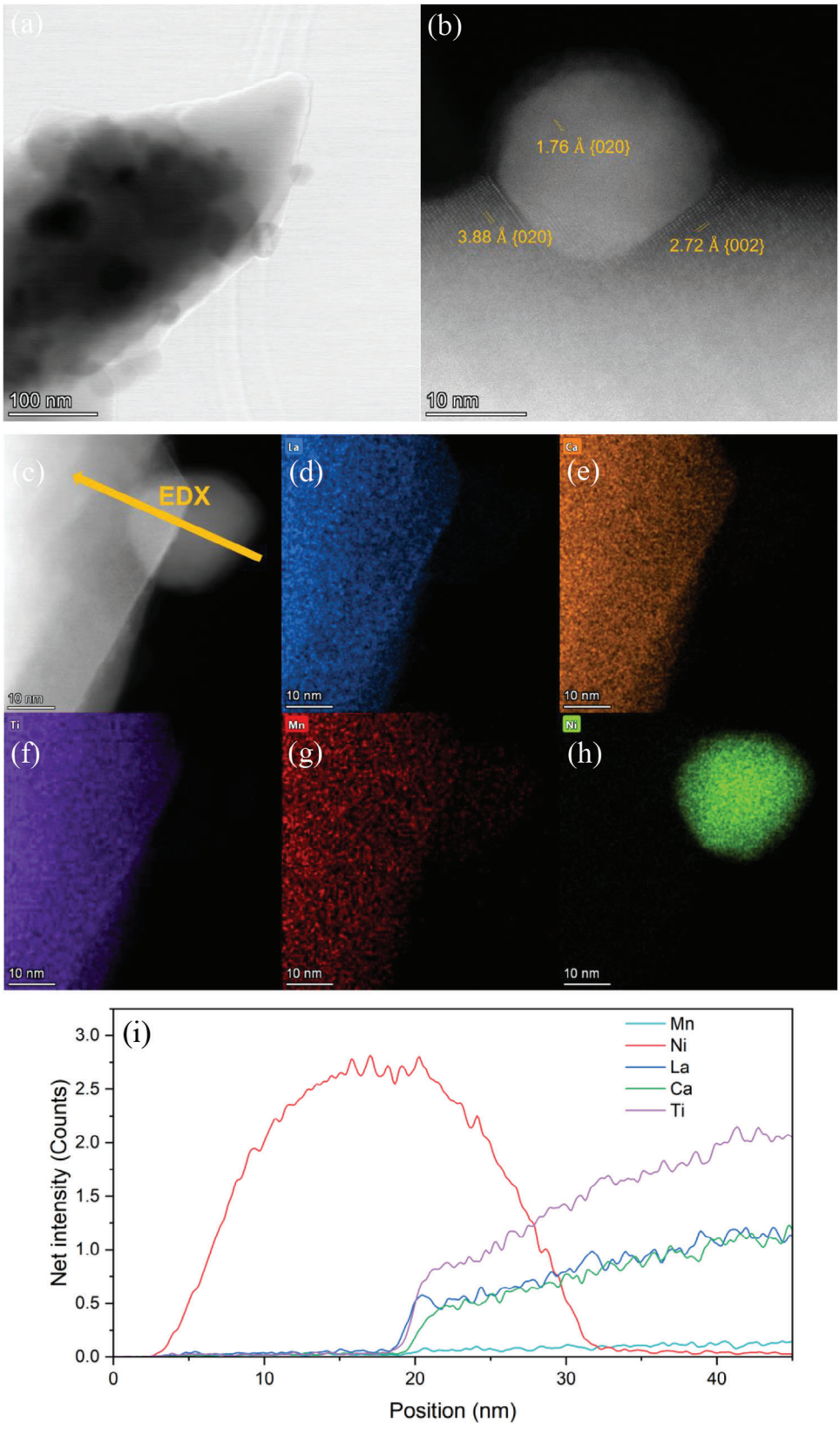

Figure 2. Scanning transmission electron microscopic analysis of reduced LCNMT5 powder. a) Dark-field STEM image. b) HAADF-STEM image. EDX element distribution diagram: c) HAADF-STEM, d) La element, e) Ca element, f) Ti element, g) Mn element, and h) Ni element. i) EDX line scan of the exsolved nanoparticle and the perovskite outer layers.

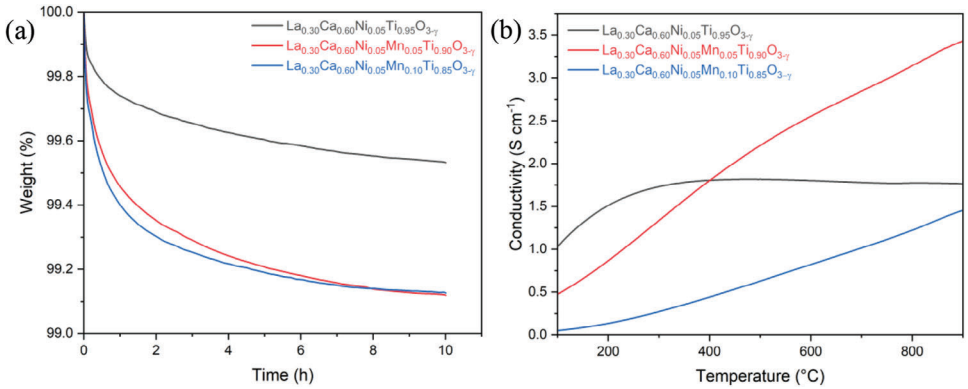

Figure 3. a) TGA experiments recorded during the reduction of the as-synthesized $La_{0.3}Ca_{0.6}Ni_{0.05}Mn_xTi_{0.95-x}O_{3-\gamma}$ ($x = 0$, 0.05, 0.10) samples in 5% H_2/N_2 at 900 °C for 10 h. b) Temperature dependence of the conductivity of reduced $La_{0.3}Ca_{0.6}Ni_{0.05}Mn_xTi_{0.95-x}O_{3-\gamma}$ ($x = 0$, 0.05, 0.10) bars in 5% H_2/N_2.

Further investigations will be essential to comprehensively understand the potential Mn exsolution from titanium-based perovskites.

To investigate the oxygen deficiency of the perovskites during reduction, thermogravimetric analysis (TGA) was carried out for the as-prepared $La_{0.3}Ca_{0.6}Ni_{0.05}Mn_xTi_{0.95-x}O_{3-\gamma}$ ($x = 0$, 0.05, 0.10) powders in 5% H_2/N_2 at 900 °C (**Figure 3**a). Since no additional volatile species or compounds are expected to be formed during the reduction process, the total weight loss observed through the TGA measurements can be ascribed to the net loss of oxygen resulting from the in situ exsolution of Ni metal nanoparticles, the reduction of Ti^{4+}, and the reduction of $Mn^{4+/3+}$. The weight loss of the compounds and their corresponding oxygen deficiency (δ) generated during the reduction are summarized in Table S1 (Supporting Information). The oxygen deficiency was calculated using the method described by Myung et al.[20] The mass consistently declines during the measurements for all samples, suggesting that the reduction process for these samples is not completed. The total weight loss values of LCNT, LCNMT5, and LCNMT10 are 0.468%, 0.881%, and 0.874%, respectively. Correspondingly, this equates to 0.0475, 0.0893, and 0.0885 oxygen per formula unit for each material. The significant difference in the oxygen deficiency generated upon reduction between LCNT and LCNMT5 indicates that Mn dopants enhance the overall reducibility of the perovskite compound. This observation is in agreement with XRD and SEM results, which show that the Mn-doped samples have a higher number of exsolved Ni nanoparticles on the surface of the perovskite substrate. However, a further increase in the Mn doping level to 10% seems to have no impact on the total oxygen deficiency formed. Despite the unchanged total oxygen deficiency, a higher Mn doping level results in a more rapid weight loss during the initial 8 h, after which both Mn-doped samples approach similar levels.

The electrical conductivity in 5% H_2/N_2 of pre-reduced $La_{0.3}Ca_{0.6}Ni_{0.05}Mn_xTi_{0.95-x}O_{3-\gamma}$ ($x = 0$, 0.05, 0.10) as a function of temperature is shown in Figure 3b. La-doped $CaTiO_3$ is known as an n-type semiconducting material, with its electrical conductivity predominantly governed by the concentration of the Ti^{4+}/Ti^{3+} redox couple.[31,32] The sample of $La_{0.3}Ca_{0.6}Ni_{0.05}Ti_{0.95}O_{3-\gamma}$ exhibits an insulator-metal transition at ≈500 °C. Below this temperature, the electrical conductivity increases with rising temperature, whereas above 500 °C, it decreases as the temperature continues to increase. A similar phenomenon has been observed by other researchers in the case of La-doped $SrTiO_3$.[33] It is important to mention that the contribution of exsolved Ni metal nanoparticles to the overall conductivity is likely minimal due to the absence of a continuous conductive network formed by these nanoparticles.[34] Upon introducing Mn dopants into the perovskite lattice, the samples exhibit semiconducting behavior across the entire temperature range, consistent with findings reported in previous studies.[35,36] The reduced $La_{0.3}Ca_{0.6}Ni_{0.05}Mn_{0.05}Ti_{0.90}O_{3-\gamma}$ sample displays a considerably enhanced conductivity of 3.42 S cm^{-1} compared to the reduced $La_{0.3}Ca_{0.6}Ni_{0.05}Ti_{0.95}O_{3-\gamma}$ sample, which exhibits a conductivity of 1.76 S cm^{-1} at 900 °C. Li et al. reported that when the partial pressure of oxygen falls below 10^{-15} atm, the conductivity of $(La_{0.2}Sr_{0.8})(Ti_{0.9}Mn_{0.1})O_{3-\gamma}$ and $(La_{0.2}Sr_{0.8})_{0.9}(Ti_{0.9}Mn_{0.1})_{0.9}Ni_{0.1}O_{3-\gamma}$ is largely enhanced with more of Ti reduced from the +4 to the +3 oxidation state.[36] Therefore, this improvement could be attributed to the lower coordination number of Mn, which not only facilitates the reduction of Ni but also promotes the reduction of Ti^{4+} to Ti^{3+}, consequently leading to an increase in charge carrier concentration and improving electrical conductivity. However, when the Mn doping level reaches 10%, a decline in conductivity is observed. This decrease is likely caused by the excessive Mn doping disrupting the B-site sublattice, ultimately impairing the Ti-O-Ti percolation that dominates electrical conductivity.[37]

2.2. Electrochemical Performance of a Single Cell

2.2.1. Cathode Microstructure: Impact on Cell Performance and Electrochemical Reduction

The impact of the cathode microstructure on the cell performance and the relationship between the microstructure and the electrochemical reduction (ER) result are investigated.

Each perovskite material $La_{0.3}Ca_{0.6}Ni_{0.05}Mn_xTi_{0.95-x}O_{3-\gamma}$ ($x = 0$, 0.05, 0.10) was used to prepare three individual cells. These cells, which used the perovskite materials as the cathode, were then sintered at varying

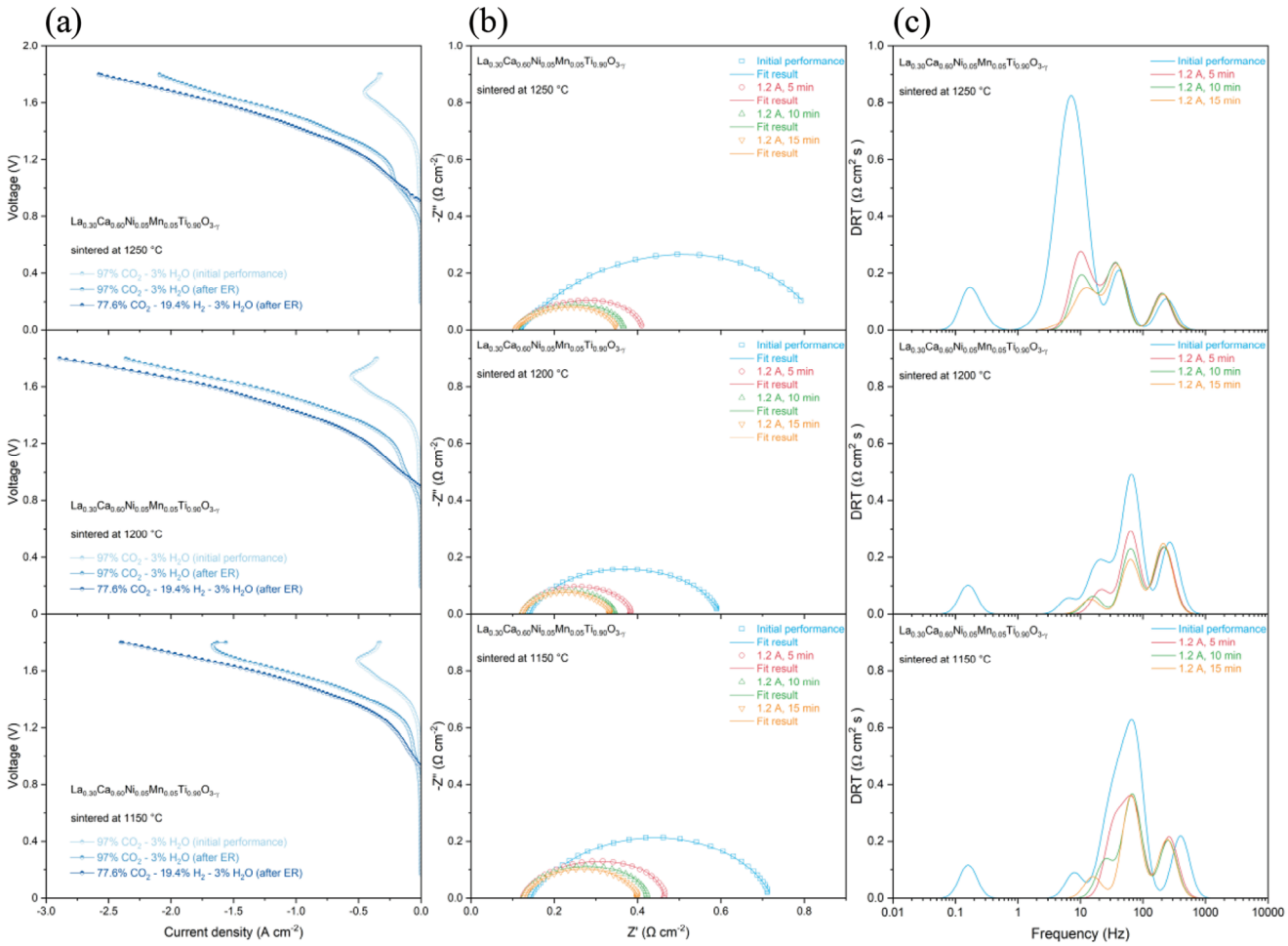

Figure 4. Electrochemical performance of LCNMT5 cells at 900 °C. a) *I–V* curves in various feeds. b) Nyquist plots in 97% CO_2 – 3% H_2O at a bias voltage of 1.4 V. c) The corresponding DRT analysis of these spectra.

temperatures. The anode ($Zr_{0.89}Sc_{0.10}Ce_{0.01}O_{2-\gamma}$-$(La_{0.8}Sr_{0.2})_{0.95}MnO_{3-\gamma}$/$(La_{0.8}Sr_{0.2})_{0.95}MnO_{3-\gamma}$) and electrolyte ($Zr_{0.89}Sc_{0.10}Ce_{0.01}O_{2-\gamma}$) remained identical across all cells. All cells underwent an identical electrochemical reduction process at a current of 1.2 A for a total of 15 min in 97% CO_2 – 3% H_2O, with each cycle lasting 5 min. To evaluate the effectiveness of the electrochemical reduction of the cathode toward CO_2 electrolysis, electrochemical impedance spectroscopy (EIS) was conducted to measure the initial performance prior to the reduction treatment and also after each electrochemical reduction cycle. *I–V* curves were also obtained before and after the electrochemical reduction process to provide further insights into the cell performance. For all the cells, regardless of the sintering temperature, the *I–V* curves demonstrate a significant improvement following the electrochemical reduction treatment (see **Figure 4** for LCNMT5, Figure S6 (Supporting Information) for LCNT and Figure S7 (Supporting Information) for LCNMT10). Cells constructed from each material display a different trend in the EIS results. The R_s and R_p values of all these cells before and after each electrochemical reduction cycle are graphically represented in Figure S8 (Supporting Information) and also summarized in Table S2 (Supporting Information) for LCNT, Table S3 (Supporting Information) for LCNMT5 and Table S4 (Supporting Information) for LCNMT10. The microstructures of cathodes, $La_{0.3}Ca_{0.6}Ni_{0.05}Mn_xTi_{0.95-x}O_{3-\gamma}$ (x = 0, 0.05, 0.10), sintered at varied temperatures, are presented in Figure S9 (Supporting Information).

Three different sintering temperatures, 1150, 1200, and 1250 °C, were employed for the LCNT cells. The LCNT cell sintered at 1200 °C (see Figures S6 and S8a, Supporting Information) initially outperforms the one sintered at 1250 °C, showing ohmic resistance (R_s) and polarization resistance (R_p) of 0.131 and 0.643 Ω cm^2, respectively. The 1250 °C-sintered cell starts with R_s and R_p values of 0.123 and 0.882 Ω cm^2, respectively. However, following a 15 min electrochemical reduction process, the performance of the 1250 °C-sintered LCNT cell surpasses that of its sintered at 1200 °C. The R_s and R_p values for the 1200 °C-sintered LCNT cell decrease to 0.116 and 0.215 Ω cm^2, respectively, while the 1250 °C-sintered LCNT cell exhibits reduced R_s and R_p values of 0.112 and 0.209 Ω cm^2, respectively. The better initial performance of the 1200 °C-sintered cell is likely attributed to its higher porosity and better microstructure. On the other hand, the denser microstructure of the 1250 °C-sintered LCNT cell appears to benefit the electrochemical reduction

process, leading to superior cell performance after the reduction process. It is also worth noting that the R_s value of the 1250 °C-sintered LCNT cell is slightly lower than that of the 1200 °C-sintered LCNT cell, suggesting improved physical and electrical contact between the electrode and electrolyte at higher sintering temperatures. This observation is in agreement with the findings reported by Jørgensen et al. and Sasaki et al.[38,39] The microstructure of the 1300 °C-sintered LCNT cell is too dense, leading to insufficient active sites (triple phase boundary) for the reaction to occur. Despite demonstrating the most significant R_p improvement and the smallest R_s, it still exhibits the worse electrochemical performance across these three cells both initially and postreduction.

LCNMT5 cells were sintered at three different temperatures: 1150, 1200, and 1250 °C. These temperatures are lower than those employed for LCNT cells, primarily due to the enhanced sintering effect contributed by the Mn dopants.[40] In contrast to the observations for LCNT cells, the LCNMT5 cells present a different relationship between sintering temperature and their initial performance. The cell sintered at 1200 °C achieves the best initial performance, outperforming the one sintered at the lowest temperature of 1150 °C, as shown in Figure 4. A comparison of microstructures (Figure S9, Supporting Information) reveals that the LCNMT5 electrode sintered at 1150 °C has some isolated round-shaped grains in the electrode. These grains are in contact with neighboring grains, a feature not observed in the LCNT electrode sintered at the lowest temperature of 1200 °C. This could potentially be ascribed to incomplete sintering of the LCNMT5 electrode at 1150 °C, which in turn, negatively impacts the cell performance.[38] The initial R_s values for the LCNMT cells sintered at 1150, 1200, and 1250 °C are 0.141, 0.139, and 0.118 Ω cm^2, respectively. Upon undergoing the first, second, and third cycles of electrochemical reduction, the R_s values for the 1150 °C-sintered LCNMT5 cell change to 0.123, 0.125, and 0.128 Ω cm^2, respectively. An increase in the R_s value is observed after the second reduction cycle. In contrast, the LCNMT5 cells sintered at higher temperatures show degradation in R_s values after the third reduction cycle. Specifically, after the first, second, and third reduction cycles, the R_s values for the cell sintered at 1200 °C are 0.122, 0.120, and 0.122 Ω cm^2, respectively. The corresponding R_s values for the cell sintered at 1250 °C are 0.107, 0.107, and 0.108 Ω cm^2, respectively. These findings further support that electrodes sintered at higher temperatures have a more robust interface with the electrolyte. Moreover, the degradation in R_s values is observed for the 5% Mn-doped cells following the reduction cycles, possibly attributed to the reduction of Mn^{3+} to Mn^{2+}, which causes significant changes in lattice volume. Despite the noticeable R_s degradation in the 5% Mn-doped cells, the R_p values consistently decrease following each electrochemical reduction cycle (Figure S8b and Table S3, Supporting Information).

The LCNMT10 cells were sintered at three different temperatures: 1050, 1100, and 1150 °C. 10% Mn-doped cells exhibit greater instability compared to the 5% Mn-doped cells, potentially due to the higher Mn doping level in the perovskite lattice aggregate instability (Figure S8b,c, Supporting Information). For all the LCNMT10 cells, both R_s and R_p exhibit degradation after the second cycle of electrochemical reduction, regardless of the sintering temperature (Figure S7, Supporting Information). The 1050 °C-sintered LCNNT10 cell experiences the most severe degradation. To be more specific, the R_s value initially decreases from 0.165 to 0.153 Ω cm^2, and the R_p drops from the 0.561 to 0.479 Ω cm^2 after the first reduction cycle, indicating that even with a 10% Mn doping level, a short-term reduction can still enhance the overall cell performance. However, after the second reduction cycle, both R_s and R_p values increase, reaching 0.190 and 0.518 Ω cm^2, respectively. Following the third reduction cycle, R_s and R_p values experience another significant increase, rising to 0.482 and 1.501 Ω cm^2, respectively.

To gain a deeper insight into the improved electrode process, the distribution of relaxation times (DRT) was used for deconvoluting the impedance data, as seen in Figure S6c (Supporting Information) for LCNT cells, Figure 4c for LCNMT5 cells, and Figure S7c (Supporting Information) for LCNMT10 cells. The DRT plots reveal that the cathode microstructure primarily impacts the peaks in the frequency range of 1–100 Hz, which are associated with adsorption, dissociation, and desorption processes (1–10 Hz) along with the surface diffusion process (10–100 Hz).[41,42]

Both the LCNT cell sintered at 1300 °C and the LCNMT5 cell sintered at 1250 °C exhibit high resistance to adsorption, dissociation, and desorption processes due to their dense microstructures. The peak frequencies for these processes in LCNT and LCNMT5 cells are 2.5 and 7.8 Hz, respectively. Lowering the sintering temperature for LCNT cells results in a significant shift of the peak frequency toward higher frequencies, accompanied by a reduction in peak area within the 1–100 Hz frequency range. This implies that the kinetics are accelerated due to the additional active sites for adsorption, dissociation, and desorption processes provided by a more porous microstructure. As a result, the LCNT cell sintered at the lowest temperature of 1200 °C initially exhibits superior performance.

Similar to LCNT cells, LCNMT5 cells sintered at 1200 and 1150 °C also show shifts in peak frequency toward higher ranges, along with a reduced peak area in the frequency range of 1–100 Hz, in comparison to LCNMT cells sintered at 1300 °C. This shift results in an overlap with the arc at a frequency of 70 Hz, which is typically associated with the surface diffusion process. The dominant peak at a frequency of 70 Hz for the LCNMT5 cell sintered at 1150 °C is more pronounced than for the cell sintered at 1200 °C, indicating that an incomplete sintering process could negatively impact adsorption, dissociation, desorption, and/or the surface diffusion processes. For LCNMT10 cells, overlapping peaks for adsorption, dissociation, and desorption processes with the surface diffusion process are observed across all sintering temperatures. Consistent with earlier findings, the peak continually shifts toward higher frequencies as the sintering temperature is reduced.

Following the electrochemical reduction treatment, both LCNT and LCNMT5 cells exhibit a significant decrease in peaks within the 1–100 Hz frequency range, irrespective of the sintering temperature. This observation aligns with the results from the EIS analysis. The main cause of this decrease is the formation of additional oxygen vacancies due to the reduction of Ti^{4+}, Ni^{2+}, and $Mn^{4+/3+}$ ions, which provide more active sites for the adsorption, activation, and dissociation processes. However, in the case of LCNMT10 cells, a consistent reduction in the peak area is not observed with increased electrochemical reduction duration. This is attributed to the instability caused by the high doping

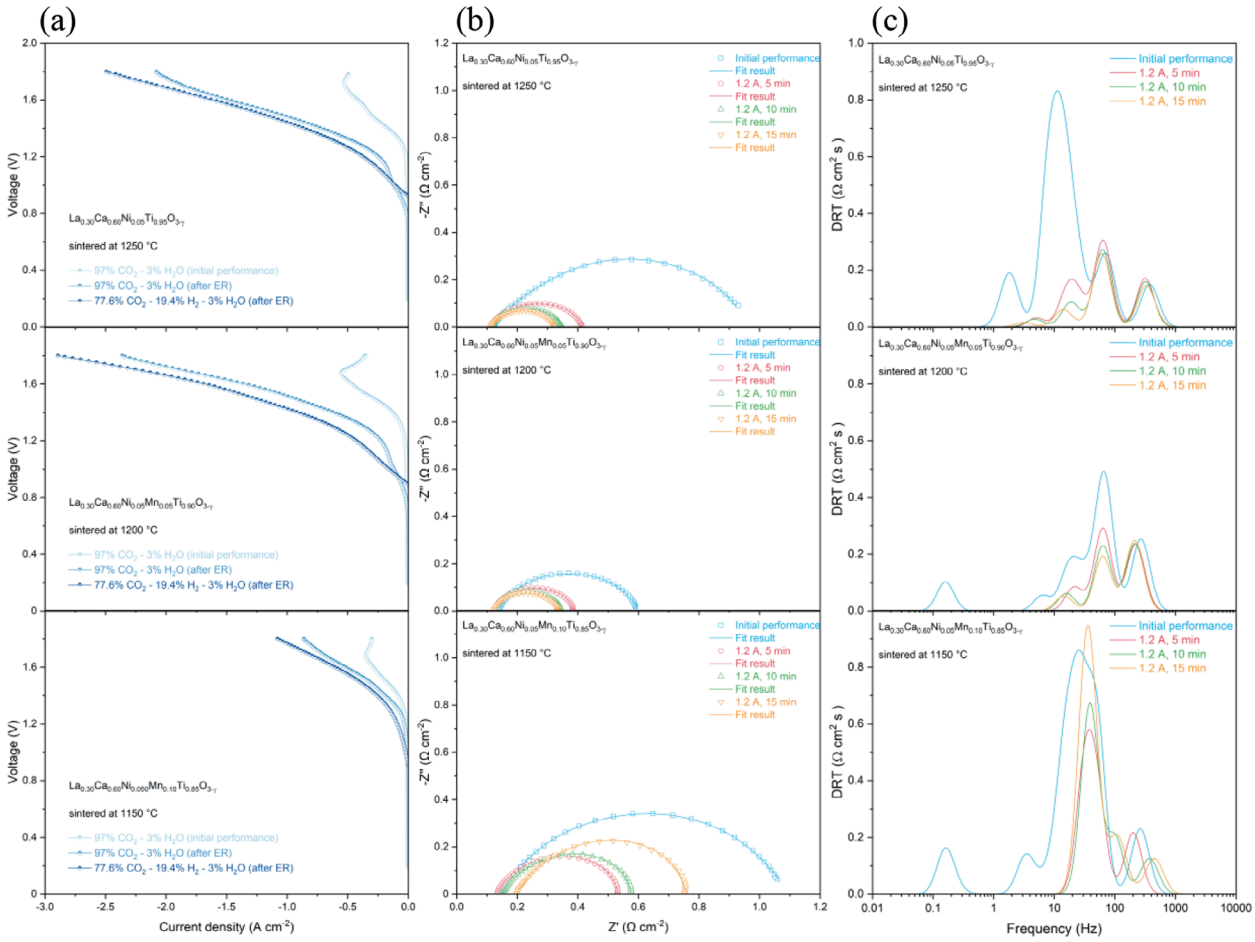

Figure 5. Electrochemical performance of $La_{0.3}Ca_{0.6}Ni_{0.05}Mn_xTi_{0.95-x}O_{3-\gamma}$ ($x = 0$, 0.05, 0.10) cells at 900 °C. a) *I–V* curves in various feeds. b) Nyquist plots in 97% CO_2 – 3% H_2O at a bias voltage of 1.4 V. c) The corresponding DRT analysis of these spectra.

level of Mn, as previously discussed. Moreover, after electrochemical reduction, dense cells exhibit a more pronounced decrease in the peak areas within the 1–100 Hz frequency range compared to porous samples. This suggests dense structures benefit more from the electrochemical reduction process, relying on it to create oxygen vacancies as active sites.

Hence, finding a balance between dense and porous structures is crucial. Dense structures can create more active sites through electrochemical reduction. In contrast, porous samples, despite generating fewer active sites during this process, intrinsically possess more active sites than dense structures. Nonetheless, incomplete sintering structures can be disadvantageous, leading to the formation of isolated round-shaped grains in the electrode. Therefore, achieving the best electrochemical performance requires an optimal balance between dense and porous structures, maximizing active site formation while minimizing potential structural drawbacks.

2.2.2. Impact of Mn Doping Levels on Electrochemical Performance

Three cells with similar microstructure, $La_{0.3}Ca_{0.6}Ni_{0.05}Mn_xTi_{0.95-x}O_{3-\gamma}$ ($x = 0$, 0.05, 0.10), are compared to evaluate the effect of Mn doping levels on the CO_2 electrolysis performance. To minimize the influence of microstructure on cell performance, a similar microstructure is selected: LCNT sintered at 1250 °C, LCNMT5 sintered at 1200 °C, and LCNMT10 sintered at 1150 °C.

Figure 5a depicts the *I–V* curves for 97% CO_2 – 3% H_2O electrolysis before and after electrochemical reduction, as well as for 77.6% CO_2 – 19.4% H_2 – 3% H_2O electrolysis after electrochemical reduction at 900 °C. Following the electrochemical reduction process, the LCNMT5 cell outperforms the LCNT cell in both 97% CO_2 – 3% H_2O and 77.6% CO_2 – 19.4% H_2 – 3% H_2O atmospheric conditions, demonstrating superior electrochemical performance. For instance, the LCNT cell achieves a current density of -2.49 A cm^{-2} in the 77.6% CO_2 – 19.4% H_2 – 3% H_2O atmosphere at an applied voltage of 1.8 V, whereas the LCNMT5 cell exhibits a higher current density of -2.89 A cm^{-2} under identical conditions. However, a further increase in the Mn doping level to 10% results in a noticeable decline in cell performance, indicating that excessive Mn doping could adversely affect the CO_2 electrolysis performance. Specifically, the current density of the cell doped with 10% Mn reaches only -1.08 A cm^{-2} at an applied voltage of 1.8 V under identical conditions. This suggests that there exists an optimal Mn doping level for this particular cell

design, beyond which performance starts to decline. All tested cells exhibit improved cell performance when H_2 is employed as the protective gas, compared to their performance evaluated in a 97% CO_2 – 3% H_2O atmosphere. This phenomenon is consistent with results reported in other studies.[43,44]

The EIS data recorded at a potential of 1.4 V in a gas atmosphere of 97% CO_2 – 3% H_2O suggests that the improved electrochemical performance of the LCNMT5 cell is primarily attributed to a reduction in R_p, as illustrated in Figure 5b. Before the electrochemical reduction, the LCNMT5 cell displays an R_p value of 0.460 Ω cm^2. This is approximately half of the 0.882 Ω cm^2 value observed for the LCNT cell, suggesting that doping with Mn can significantly facilitate the CO_2 reduction reaction. After the first, second, and third reduction cycles, the LCNT cell demonstrates R_p values of 0.304, 0.236, and 0.209 Ω cm^2, respectively. In contrast, the impact of the electrochemical reduction process on the LCNMT5 cell is more pronounced during the first reduction cycle, with this effect diminishing during the subsequent second and third cycles. The R_p values for the LCNMT5 cell after each corresponding cycle are 0.259, 0.224, and 0.209 Ω cm^2. As previously discussed, prolonged reduction time negatively impacts the performance of the Mn-doped cells. Prior to the third reduction cycle, the LCNMT5 cell demonstrates lower R_p values than those of the LCNT cell. Although the LCNT and LCNMT5 cells display identical R_p values of 0.209 Ω cm^2 at 1.4 V after the third reduction cycle, the LCNMT5 still outperforms the LCNT cell at higher voltages according to the *I–V* curves. Upon further increasing the Mn doping level to 10%, the initial R_p value rises to 0.927 Ω cm^2. In comparison to the LCNMT5 cell, the R_p value is higher, indicating that additional Mn doping is not beneficial for enhancing cell performance, which aligns with the *I–V* results. The R_p value increases after the second reduction cycle, implying that the higher Mn concentration in the electrode increases its instability, as previously discussed.

To further explore the impact of the Mn dopants on the CO_2 electrolysis performance, the DRT plots of LCNT, LCNMT5, and LCNMT10 are compared in Figure 5c. Upon introducing 5% Mn into the cathode, a significant reduction in the intensity of peaks within the 1–100 Hz segment is observed. Moreover, a shift in the frequency of these peaks toward the higher frequencies is noted. The dominant frequency peak of LCNT, originally at 11 Hz, migrates to higher frequencies in the LCNMT5, possibly merging with the peak around 70 Hz. This observation is likely attributable to the inherent tendency of Mn to exhibit a lower coordination number within the perovskite lattice. This characteristic could lead to an increase in oxygen vacancies and promote oxide-ion migration. Consequently, it may enhance the reaction kinetics within the electrode and expedite processes like CO_2 adsorption, dissociation, and activation on the cathode surface.

Throughout the electrochemical reduction process, the LCNT cell exhibits a pronounced decrease in the peak area within the 1–100 Hz frequency range. While the LCNMT5 cell also shows a decrease in the same peak area, the reduction is less pronounced compared to the LCNT cell. The decrease in peak area after the electrochemical reduction process can be attributed to the increase in oxygen vacancies arising from the reduction of B-site ions, as mentioned earlier.

When the Mn doping level is increased further to 10%, a detrimental impact on performance is seen, particularly in the 1–100 Hz frequency segment. Here, the peaks demonstrated a significant increase following a 10 min electrochemical reduction treatment, which is consistent with the findings from the EIS analysis. Notably, the initial peak area of LCNMT10 cell in the 1–100 Hz frequency range is larger than that of the LCNMT5, further reinforcing the conclusion that increasing the doping level of Mn is unable to enhance cell performance. In addition, an arc featuring a summit frequency of 0.15 Hz appeared in the initial performance measurement for both Mn-doped cells, which could be attributed to gas conversion and/or gas diffusion.[41] Following a 5 min electrochemical reduction treatment, the peak disappeared for both cells, suggesting that the surface of the cathode should be decorated with exsolved nanoparticles after this treatment. The presence of nanoparticles could increase the number of active sites, which in turn could enhance the gas–solid interface. This enhancement could facilitate more efficient gas conversion and diffusion processes.

In summary, the improved electrolysis performance achieved through 5% Mn doping aligns with the impedance spectroscopy findings, indicating that substituting Mn at the Ti-site alongside an active transition metal (e.g., Ni) presents a promising approach for enhancing catalytic activity in CO_2 electrolysis, whereas excessive Mn doping appears to aggravate the instability of the cell, thereby negatively affecting the overall performance of the electrolysis cell.

The long-term stability of $La_{0.3}Ca_{0.6}Ni_{0.05}Mn_{0.05}Ti_{0.90}O_{3-\gamma}$ | $Zr_{0.89}Sc_{0.10}Ce_{0.01}O_{2-\gamma}$ | $Zr_{0.89}Sc_{0.10}Ce_{0.01}O_{2-\gamma}$-$(La_{0.8}Sr_{0.2})_{0.95}$-$MnO_{3-\gamma}$ | $(La_{0.8}Sr_{0.2})_{0.95}MnO_{3-\gamma}$ electrolysis cell was further carried out at 900 °C under an applied voltage of 1.2 V. The cell steadily outputted a stable current density of −0.389 A cm^{-2} during the entire 133 h operation, which demonstrates that the cell possesses good durability for long-term application, as illustrated in Figure S10 (Supporting Information). The current density from the stability test is consistent with the performance response shown in Figure 5a. Additionally, the SEM image of the LCNMT5 electrode following the stability test, as presented in Figure S11 (Supporting Information), shows that no significant changes in the particle size and population of exsolved nanoparticles.

3. Conclusion

In conclusion, this study examined the influence of Mn doping on $La_{0.3}Ca_{0.6}Ni_{0.05}Mn_xTi_{0.95-x}O_{3-\gamma}$ (x = 0, 0.05, 0.10) perovskite materials and the microstructure of cathodes, both of which are crucial to the performance of CO_2 electrolysis in solid oxide electrolysis cells. The XRD and SEM confirmed that the Mn dopants promoted Ni exsolution from the perovskite lattice. A strong interaction between exsolved Ni nanoparticles and the perovskite matrix was verified through TEM and EDX analyses. Furthermore, it was found that these Mn dopants improved the electrical conductivity, with 5% determined as the optimal Mn doping level. The study found optimizing the microstructure is essential, as a balance between dense and porous structures is necessary for achieving optimal electrochemical performance. While dense structures have the ability to generate a larger number of active sites through the electrochemical reduction process, porous structures, by their very nature, inherently contain more of these

active sites despite producing fewer during the same process. It is important to note that excessively porous structures may pose drawbacks and negatively impact cell performance. Moreover, while Mn doping can significantly enhance cell performance, it should be noted that excessive doping levels may have a negative effect on cell stability. An optimal Mn doping level of 5% was identified in the study, which was found to enhance cell performance by creating more oxygen vacancies and Ni nanoparticles. Compared to the LCNT cell, the LCNMT5 cell demonstrated higher current densities at 900 °C and 1.8 V of −2.89 A cm^{-2} in 77.6% CO_2 – 19.4% H_2 – 3% H_2O atmosphere. Overall, the results suggested that optimizing both microstructure and Mn doping levels could be promising approaches for improving the performance of CO_2 electrolysis cells.

Building on the insights gained from this study, further research and improvements can be explored. The following perspectives provide potential strategies to address the identified challenges and limitations.

For instance, shortening the electrochemical reduction treatment time could potentially improve the stability of Mn-doped cells. In addition, a short electrochemical reduction time could be sufficient to fully activate the Mn-doped cells. This can be attributed to the enhanced oxygen ion migration in Mn-doped materials, which consequently increases their reducibility.

Moreover, a charge compensation strategy can be employed to increase Ni doping level while maintaining the same Mn doping level. In this case, incorporating more Ni^{2+} into the perovskite will shift the primary valence of Mn toward 4+, consequently decreasing the number of Mn ions reduced from 3+ to 2+. This approach may help mitigate the adverse effects of Mn reduction on the stability and further increase the overall performance of the electrolysis cell.

4. Experimental Section

Materials Preparation: All $La_{0.3}Ca_{0.6}Ni_{0.05}Mn_xTi_{0.95-x}O_{3-\gamma}$ (x = 0, 0.05, 0.10) samples were prepared by the solid-state synthesis route. Using $La_{0.3}Ca_{0.6}Ni_{0.05}Mn_{0.05}Ti_{0.90}O_{3-\gamma}$ as a representative example, specific oxides and carbonated were initially pre-calcined at various temperatures (La_2O_3, 800 °C; TiO_2, 300 °C; $CaCO_3$, 300 °C) to ensure accurate stoichiometry. An appropriate stoichiometric ratio of La_2O_3 (Pi-Kem, 99.99%), TiO_2 (Alfa Aesar, 99.6%), $CaCO_3$ (Alfa Aesar, 99.5%), $Ni(NO_3)_2$*$6H_2O$ (Acros, 99%), $Mn(NO_3)_2$*$6H_2O$ (Alfa Aesar, 98%) were weighed. Subsequently, the mixture was mixed with ethanol and ≈0.05 wt% Hypermer KD1 dispersant, followed by sonication to break down agglomerates and homogenize the mixture. The ethanol evaporated at 70 °C with continuous stirring. The dried powders underwent calcination at 1000 °C for 12 h to decompose the carbonated and initiate perovskite phase formation. The calcined powder was subjected to ball milling at 400 rpm for 2 h using ethanol as a solvent. The mixture was dried at 70 °C and uniaxially pressed into pellets, which were subsequently sintered in air at 1450 °C for 12 h to form a perovskite phase. The sintered pellets were crushed and motor-grinded into smaller particles and the resulting powders were ball milled at 700 rpm for 2 h to attain the desired particle size.

Cell Fabrication: Electrolyte-supported cells with the configuration $La_{0.3}Ca_{0.6}Ni_{0.05}Mn_xTi_{0.95-x}O_{3-\gamma}$ | $Zr_{0.89}Sc_{0.10}Ce_{0.01}O_{2-\gamma}$ | $Zr_{0.89}Sc_{0.10}Ce_{0.01}O_{2-\gamma}$-$(La_{0.8}Sr_{0.2})_{0.95}MnO_{3-\gamma}$ | $(La_{0.8}Sr_{0.2})_{0.95}MnO_{3-\gamma}$ were employed to investigate and assess the electrochemical properties of CO_2 electrolysis. $La_{0.3}Ca_{0.6}Ni_{0.05}Mn_xTi_{0.95-x}O_{3-\gamma}$ (x = 0, 0.05, 0.10) powders were combined with an organic binder consisting of α-terpinol and polyvinyl butyral (PVB) to form fuel electrode slurries. Similarly, the $Zr_{0.89}Sc_{0.10}Ce_{0.01}O_{2-\gamma}$ (ScCeSZ)-$(La_{0.8}Sr_{0.2})_{0.95}MnO_{3-\gamma}$(LSM) (50:50 wt%) and LSM air electrode slurries were prepared using the same technique. Fuel electrode slurry and air electrode slurries were screen-printed on opposite sides of the commercial ScCeSZ (Kerafol, 150 µm) electrolyte. For the air electrode, LSM-ScCeSZ was initially screen-printed on the ScCeSZ electrolyte as the functional layer, followed by the screen-printing of pure LSM as the current collector layer. Subsequently, a cosintered process was conducted at 1100 °C for 2 h. The fuel electrode was fabricated using the same screen-printing process. The sintering temperature for the fuel electrodes was dependent on the specific materials. Multiple sintering temperatures were tested to optimize the fuel electrode microstructure. The electrode with a higher sintering temperature was screen-printed and calcinated first. Gold (Au) paste was used as the current collector and the single cell exhibited an active area of 0.5 cm^2.

Material Characterizations: The crystal structure of the synthesized and reduced perovskite materials was analyzed using a PANalytical Empyrean X-ray Diffractometer, operating in reflection mode with Cu Kα radiation. Rietveld refinements of the obtained diffraction patterns were carried out using the GSAS II software. The microstructure and morphology of the samples were examined using scanning electron microscopy (SEM, FEI Scios DualBeam). The crystalline structures and the element distributions of the samples were observed by a scanning transmission electron microscope (STEM, FEI Titan Themis) equipped with an energy dispersive X-ray spectroscopy (EDX) detector. Thermogravimetric analysis (TGA, Netzsch STA 449 Jupiter) was conducted on the as-synthesized perovskite materials at a temperature of 900 °C for 10 h to investigate the weight loss of the materials under a gas atmosphere of 5% H_2/N_2. Porous bars of the perovskite materials, with a density of 60%, were prepared via dry-pressing and subsequently sintered in the air for the electrical conductivity test using the DC four-probe method. Prior to conductivity measurement, the conductivity bars were reduced at 900 °C for 30 h in 5% H_2/N_2. Conductivity measurements were performed in the temperature range of 100–900 °C under a gas atmosphere of 5% H_2/N_2.

Electrochemical Measurement: The as-fabricated single cell was sealed using ceramabond (Aremco #552) and mounted onto an alumina jig for electrochemical characterization, with the air electrode exposed to ambient air. The temperature gradually increased to 900 °C. Simultaneously, a mixture of 5% H_2/N_2 was introduced into the fuel electrode at the flow rate of 50 mL min^{-1}. Once the cell reached 900 °C, the gaseous environment was switched to a humidified CO_2 atmosphere (3% H_2O), maintaining the same flow rate of 50 mL min^{-1} for the initial cell performance evaluation. The electrochemical reduction was performed by applying 1.2 A (vs air electrode) for 3 cycles, with each cycle lasting 5 min. Electrochemical impedance spectroscopy (EIS) was collected between each electrochemical reduction cycle. Subsequently, the performance of the cells after electrochemical activation was assessed using EIS and the *I–V* curve. A stability test was then conducted in the presence of humidified CO_2 at 900 °C for 133 h at an operating voltage of 1.2 V. EIS measurements were collected under an applied voltage of 1.4 V in the frequency range from 20 kHz to 1 Hz using an electrochemical working station (Solartron 1280B), with a voltage amplitude of 20 mV, while *I–V* curves were recorded across a range from open circuit voltage (OCV) to 1.6 V at a scanning rate of 10 mV s^{-1}.

Supporting Information

Supporting Information is available from the Wiley Online Library or from the author.

Acknowledgements

This work was financially supported by the Industrial Decarbonisation Research and Innovation Centre through research Grant No. EP/V027050/1. Further support was kindly provided by EPSRC under research Grant Nos. EP/L017008/1, EP/R023751/1, and EP/T019298/1.

Conflict of Interest

The authors declare no conflict of interest.

Data Availability Statement

The research dataunderpinning this publication can be accessed at https://doi.org/10.17630/6f2acc8f-95ed-47d3-b218-71358b06503e.[45]

Keywords

CO_2 electrolysis, in situ exsolution, nanoparticles, perovskites, solid oxide electrolysis cells

Received: August 21, 2023
Revised: October 19, 2023
Published online:

[1] E. D. Coyle, R. A. Simmons, *Understanding the Global Energy Crisis*, Purdue University Press, West Lafayette, IN **2014**.
[2] Y. Song, X. Zhang, K. Xie, G. Wang, X. Bao, *Adv. Mater.* **2019**, *31*, 1902033.
[3] W. Wang, L. Gan, J. P. Lemmon, F. Chen, J. T. S. Irvine, K. Xie, *Nat. Commun.* **2019**, *10*, 1550.
[4] S. Lee, S. H. Woo, T. H. Shin, J. T. S. Irvine, *Chem. Eng. J.* **2021**, *420*, 127706.
[5] W. L. Becker, R. J. Braun, M. Penev, M. Melaina, *Energy* **2012**, *47*, 99.
[6] G. Cinti, A. Baldinelli, A. Di Michele, U. Desideri, *Appl. Energy* **2016**, *162*, 308.
[7] B. Shri Prakash, S. Senthil Kumar, S. T. Aruna, *Renewable Sustainable Energy Rev.* **2014**, *36*, 149.
[8] M. S. Khan, S.-B. Lee, R.-H. Song, J.-W. Lee, T.-H. Lim, S.-J. Park, *Ceram. Int.* **2016**, *42*, 35.
[9] S. Tao, J. T. S. Irvine, *Chem. Rec.* **2004**, *4*, 83.
[10] M. C. Verbraeken, T. Ramos, K. Agersted, Q. Ma, C. D. Savaniu, B. R. Sudireddy, J. T. S. Irvine, P. Holtappels, F. Tietz, *RSC Adv.* **2015**, *5*, 1168.
[11] Y. Zheng, Z. Chen, J. Zhang, *Electrochem. Energy Rev.* **2021**, *4*, 508.
[12] L. Thommy, O. Joubert, J. Hamon, M.-T. Caldes, *Int. J. Hydrogen Energy* **2016**, *41*, 14207.
[13] S. Jo, H. G. Jeong, Y. H. Kim, D. Neagu, J.-H. Myung, *Appl. Catal., B* **2021**, *285*, 119828.
[14] C. Zhao, Y. Li, W. Zhang, Y. Zheng, X. Lou, B. Yu, J. Chen, Y. Chen, M. Liu, J. Wang, *Energy Environ. Sci.* **2020**, *13*, 53.
[15] X. Xi, X.-W. Wang, Y. Fan, Q. Wang, Y. Lu, J. Li, L. Shao, J.-L. Luo, X.-Z. Fu, *J. Power Sources* **2021**, *482*, 228981.
[16] D. Neagu, G. Tsekouras, D. N. Miller, H. Ménard, J. T. S. Irvine, *Nat. Chem.* **2013**, *5*, 916.
[17] J. Feng, J. Qiao, W. Wang, Z. Wang, W. Sun, K. Sun, *Electrochim. Acta* **2016**, *215*, 592.
[18] Y.-F. Sun, J.-H. Li, M.-N. Wang, B. Hua, J. Li, J.-L. Luo, *J. Mater. Chem. A* **2015**, *3*, 14625.
[19] Y. Sun, J. Li, Y. Zeng, B. S. Amirkhiz, M. Wang, Y. Behnamian, J. Luo, *J. Mater. Chem. A* **2015**, *3*, 11048.
[20] J.-H. Myung, D. Neagu, D. N. Miller, J. T. S. Irvine, *Nature* **2016**, *537*, 528.
[21] Y. Zang, P. Wei, H. Li, D. Gao, G. Wang, *Electrochem. Energy Rev.* **2022**, *5*, 29.
[22] R.-B. Song, W. Zhu, J. Fu, Y. Chen, L. Liu, J.-R. Zhang, Y. Lin, J.-J. Zhu, *Adv. Mater.* **2020**, *32*, 1903796.
[23] J. C. Ruiz-Morales, J. Canales-Vázquez, C. Savaniu, D. Marrero-López, W. Zhou, J. T. S. Irvine, *Nature* **2006**, *439*, 568.
[24] W. Qi, Y. Gan, D. Yin, Z. Li, G. Wu, K. Xie, Y. Wu, *J. Mater. Chem. A* **2014**, *2*, 6904.
[25] L. Ye, M. Zhang, P. Huang, G. Guo, M. Hong, C. Li, J. T. S. Irvine, K. Xie, *Nat. Commun.* **2017**, *8*, 14785.
[26] R. D. Shannon, *Acta Crystallogr., A* **1976**, *32*, 751.
[27] K. R. Poeppelmeier, M. E. Leonowicz, J. M. Longo, *J. Solid State Chem.* **1982**, *44*, 89.
[28] B. Hua, M. Li, Y.-F. Sun, J.-H. Li, J.-L. Luo, *ChemSusChem* **2017**, *10*, 3333.
[29] S. Liu, Q. Liu, J.-L. Luo, *ACS Catal.* **2016**, *6*, 6219.
[30] Y. Zheng, J. Wang, B. Yu, W. Zhang, J. Chen, J. Qiao, J. Zhang, *Chem. Soc. Rev.* **2017**, *46*, 1427.
[31] T. Bak, J. Nowotny, C. C. Sorrell, M. F. Zhou, E. R. Vance, *J. Mater. Sci.: Mater. Electron.* **2004**, *15*, 635.
[32] U. Balachandran, N. G. Eror, *J. Mater. Sci.* **1982**, *17*, 1795.
[33] S. R. Popuri, A. J. M. Scott, R. A. Downie, M. A. Hall, E. Suard, R. Decourt, M. Pollet, J.-W. G. Bos, *RSC Adv.* **2014**, *4*, 33720.
[34] T. Zhu, H. Troiani, L. V. Mogni, M. Santaya, M. Han, S. A. Barnett, *J. Power Sources* **2019**, *439*, 227077.
[35] J. C. Ruiz-Morales, J. Canales-Vázquez, C. Savaniu, D. Marrero-López, P. Núñez, W. Zhou, J. T. S. Irvine, *Phys. Chem. Chem. Phys.* **2007**, *9*, 1821.
[36] Y. Li, K. Xie, S. Chen, H. Li, Y. Zhang, Y. Wu, *Electrochim. Acta* **2015**, *153*, 325.
[37] D. Neagu, J. T. S. Irvine, *Chem. Mater.* **2011**, *23*, 1607.
[38] K. Sasaki, J.-P. Wurth, R. Gschwend, M. Gödickemeier, L. J. Gauckler, *J. Electrochem. Soc.* **1996**, *143*, 530.
[39] M. Jørgensen, *Solid State Ion.* **2001**, *139*, 1.
[40] J. A. Cerri, E. R. Leite, D. Gouvêa, E. Longo, J. A. Varela, *J. Am. Ceram. Soc.* **1996**, *79*, 799.
[41] S. D. Ebbesen, M. Mogensen, *J. Power Sources* **2009**, *193*, 349.
[42] M. J. Jørgensen, M. Mogensen, *J. Electrochem. Soc.* **2001**, *148*, A433.
[43] Z. Li, M. Peng, Y. Zhu, Z. Hu, C.-W. Pao, Y.-C. Chang, Y. Zhang, Y. Zhao, J. Li, Y. Sun, *J. Mater. Chem. A* **2022**, *10*, 20350.
[44] V. Kyriakou, D. Neagu, E. I. Papaioannou, I. S. Metcalfe, M. C. M. Van De Sanden, M. N. Tsampas, *Appl. Catal., B* **2019**, *258*, 117950.
[45] N. Zhang, A. Naden, L. Zhang, X. Yang, P. Connor, J. Irvine, Enhanced CO2 Electrolysis Through Mn Substitution Coupled with Ni Exsolution in Lanthanum Calcium Titanate Electrodes. Dataset. University of St Andrews Research Portal, **2023**, https://doi.org/10.17630/6f2acc8f-95ed-47d3-b218-71358b06503e.